IEEE Access
Multidisciplinary ⋮ Rapid Review ⋮ Open Access Journal

Received March 4, 2021, accepted March 18, 2021, date of publication March 29, 2021, date of current version April 12, 2021.

Digital Object Identifier 10.1109/ACCESS.2021.3069444

On the Tuning of Fractional Order Resonant Controllers for a Voltage Source Converter in a Weak AC Grid Context

MARTA HARO-LARRODE[1], GILBERT BERGNA-DIAZ[2], (Member, IEEE), PABLO EGUIA[3], (Member, IEEE), AND MAIDER SANTOS-MUGICA[4]

[1]Department of Electrical Engineering, CIRCE Institute, University of Zaragoza, 50018 Zaragoza, Spain
[2]Department of Electric Power Engineering, Norwegian University of Science and Technology, 7491 Trondheim, Norway
[3]Department of Electrical Engineering, University of the Basque Country, 48013 Bilbao, Spain
[4]Tecnalia, Basque Research and Technology Alliance (BRTA), E-48160 Derio, Spain

Corresponding author: Marta Haro-Larrode (mharolarrode@unizar.es)

This work was supported by the Basque Government through the Project of Research Group GISEL under Grant IT1083-16. Besides, TECNALIA is a ''CERVERA Technology Centre of Excellence'' recognised by the Ministry of Science and Innovation.

ABSTRACT This paper proposes a method for tuning the fractional exponent of different types of fractional order resonant controllers for a voltage source converter in a weak AC grid context. The main objective is to ensure the stability of the controlled system in a weak AC grid environment and to achieve an adequate dynamic response under disturbances. Therefore, six commonly used integer order proportional resonant (PR) control structures are selected from the literature and compared with each other according to their frequency behaviour. Afterwards, a rational approximation for the fractional order term is selected based on continuous fraction expansion technique. The inclusion of a fractional exponent in each integer order PR structure generates the fractional order proportional resonant (FPR) control transfer functions. Once the FPR controllers have been obtained, their closed-loop responses are tested via eigenvalue trajectory analysis. For each FPR control structure, a range of the fractional exponent that ensures stability is obtained. The conclusions of eigenvalue trajectory analysis are tested by implementing the FPR control structures in an specific application consisting in a modular multi-level converter (MMC) connected to a weak AC grid with adjustable short-circuit ratio. By means of time-domain simulations, not only the previous eigenvalue analyses are validated, but also new tuning criteria are given for the fractional exponent in combination with other control parameters, such as the damping frequency and the inductance of the complementary feedback branch. Moreover, a sensitivity analysis of the tuning criteria is carried out for other sizes of the AC filter inductance.

INDEX TERMS Stability analysis, fractional order resonant control, frequency analysis, weak AC grid.

I. INTRODUCTION

Advanced energy conversion systems with multiple electrical ports and their control approaches are nowadays in the spotlight of the current research trends in electrical engineering. The main reasons behind their growing role are, above all, the need of increasing efficiency and flexibility of energy converters in a context where renewable energy sources (RES) are more and more distributed [1], which in turn, acts as an important driver for the digitalisation of electric power system models in the energy sector [2].

The associate editor coordinating the review of this manuscript and approving it for publication was Mira Naftaly.

Digital models for dynamic and transient simulation of energy conversion systems are becoming the cornerstone of research in multi-port advanced conversion systems in order to predict their behaviour in unexpected but ever more and more frequent circumstances. In this vein, the weakening of AC grids due to dynamic impact of nearby grids with high content of power electronic-based RES [3] or challenges for inertial response [4] are scenarios that may command a new design of control schemes or new parameterisations. Therefore, simulations are a powerful tool to study such scenarios and redesign control schemes, as they allow to work with simplified representations of multi-port energy conversion systems for large system studies [5].

Besides, with the increasingly frequent cooperative control among devices and in the advent of multi-purpose control systems and strategies [6], the tuning of control parameters of devices is gaining complexity, as resonances between control systems or between control systems and power equipment may appear [7]. Moreover, the exploration of extra degrees of freedom in controllers provided by additional parameters, other than their proportional or integral control parameters, adds flexibility to cope with these complexities.

Among these multi-port advanced energy conversion systems, the voltage source converter (VSC) stands out over its competitor, the current source converter (CSC), as it is able to achieve a separate control of active and reactive power, manage a higher control level of DC grids and provide black-start capability [3], [8]. The control schematics of VSCs are usually composed by two stages: on the one hand, the outer loop stage, which is aimed at controlling the active, reactive power and/or DC voltage, and on the other hand, the inner loop stage, whose objective is the control of currents at the point of common coupling (PCC) [3], [9], [10]. These currents, or at least a transformed version of them, made through the modulation or insertion indices, are ultimately used to control the VSC. An specific VSC is the modular multilevel converter (MMC), which is particularly employed in high-voltage direct current (HVDC) systems due to its benefits over the two-level VSC, among which the modularity, reduced losses and scalability are listed [11]–[13].

According to the existing literature, the inner current control schemes most widely employed are the proportional integral (PI) controllers due to their simpler implementation, whereas proportional resonant (PR) schemes have been tested to provide improvements regarding their response under unbalanced faults in comparison to PI controllers [14]–[17], at the cost of certain dependency to frequency changes. The dependency of PR controllers on frequency changes has been vastly studied in [18]–[20].

To the best knowledge of the authors, there are three different ways to reduce the dependency to frequency changes of an ideal topology of a PR controller and thus improve its properties.

A first way is to modify the transfer function of the ideal PR controller topology, either by adding a first order damping term in the denominator or by including a second order term that multiplies the proportional constant. Both modifications of the ideal PR topology are called, respectively, the non-ideal and the complex-vector PR controllers, and they reduce the dependency of the ideal PR controller to frequency changes, being the complex-vector topology the one which achieves the largest reduction. However, complex-vector PR controller may present stability issues if no voltage decoupling branches are provided [3], [18].

A second way to reduce the sensitivity of the PR controller to frequency variations, is the inclusion of different feedback complementary branches, giving rise to PRXF, PRXC and PRX2 topologies. Among them, PRXF provides a lower sensitivity to frequency changes compared to ideal PR controller in direct sequence. However, the sensitivity to frequency changes is much higher in inverse sequence. In contrast, PRXC reduces the sensitivity with respect to ideal PR controller but not as much as the PRXF controller. Furthermore, PRXC topology is not able to work with inverse sequence currents. Eventually, PRX2 controller achieves the largest reduction of dependency to frequency compared to PRXF or PRXC, and achieves this in both direct and inverse sequences [9], [19], [20].

A third way to reduce their dependency on frequency is to include a fractional order term in their transfer function. For this purpose, there are different approximations that have been employed to represent a fractional order term, according to [21], [22]. In [23], a fractional order resonant controller was introduced and their implementation showed robustness against fluctuations in frequency and an improved transient response, although a limited range of fractional exponent (lower than 1) was tested and the controller was not tested in a weak AC grid environment. Furthermore, they did neither consider fractional order PR controller topologies, other than the fractional ideal PR scheme, nor contemplated variations in the AC filter inductance while performing the analysis. The authors in [24], [25] developed a concept of fractional order PR controller by selecting the Chareff's approximation to represent the fractional order term and researched on a tuning methodology for improving the phase delay for a wide energy range. Their study was mainly focused on the fractional order topologies coming from PI and ideal PR configurations, and the fractional order PR configuration was also extended for harmonic compensation. However, they did not implement their methodology for fractional exponents lower than 1 and did neither look for sources of instability due to AC grid weakness, nor considered other fractional order PR configurations different from PR ideal topology. Besides, the authors in [26] developed a fractional order controller for frequency regulation in a multi-area power system, based on employing a hybrid fractional order controller for load frequency control, in combination with the fractional order proportional integral controller for battery management, showing robustness against the variation of physical parameters. Despite this, no resonant controller types were explored in this hybrid methodology.

The design of fractional order controllers for systems with time delays has been mostly studied in [27]–[29]. In [27], a fractional order controller was implemented in the speed control of a DC motor with time delay, and the efficiency of the fractional implementation was reported in the simulations. In [28], a generalised fractional order proportional integral derivative controller was designed according to the obtention of the biggest regional stability area, and it was reported to be useful for systems having time delays. The authors in [29] imposed frequency domain specifications, namely the gain crossover frequency, phase margin and iso-damping property, to tune the fractional order controller for a system with time delays, and the resulting controller

properly mitigated the disturbances despite the time delays.

The application of artificial intelligence algorithms to design the fractional order resonant controller has been treated in [30]–[32], where the authors studied and compared their results with those obtained with proportional integral derivative (PID) controller. While authors in [30] focused on a particle swarm optimization technique, the authors in [31] and [32] used a flower pollination algorithm to design the fractional order controller for stable and unstable systems, respectively.

There are other authors, such as [33], [34], that have focused the design of fractional order controllers on stability considerations, as proposed in the present paper. In [33], the fractional-order control strategy was based on fractional-order Lyapunov stability theory and its effectiveness was checked via numerical simulations. In [34], the authors designed the fractional order controller based on the quatitative feedback theory. According to this approach, the fractional order controller is employed to control uncertainties, and the prefilter is used to drive the system response to the desired frequency domain. The approach was implemented in a linearised two-dimensional model of a common industrial robot and was verified via simulations.

The previous works listed in the literature, [23]–[34], were mostly focused on the tuning of proportional and integral control parameters, in combination with the fractional exponent of fractional order PI, PID and ideal PR controllers. However, they did not consider other degrees of freedom present in other PR control topologies different from the ideal PR type, such as the complementary feedback branch inductance or the damping frequency. To the best knowledge of the authors, the stability diagnosis of diverse fractional order PR control topologies, via eigenvalue trajectory analysis, has not been explored yet. And much less, in a weak AC grid context. Besides, the combined tuning of the fractional exponent of these controllers with parameters, other than proportional and integral constants, has not been analysed yet.

Therefore, these previous works open a research gap not covered until now, which leads to further improvements on the tuning of fractional exponent for different fractional order proportional resonant (FPR) controllers, to ensure stability and a proper dynamic response with respect to the integer order PR controller case. Therefore, the contributions of this paper to the state of the art are listed hereafter. First, the usage of a new approximation for the fractional order term, s^{α}. This approximation can be calculated according to a systematic procedure based on the continuous fraction expansion technique, which is simple to compute compared to other approximations and yields to sufficient accuracy, as stated in [35]. Second, the configuration-based stability analysis based on the previous integer order PR topologies that already improved the properties of ideal PR controller. This approach implies that the values for fractional exponent will affect differently depending on the FPR topology under consideration. The inclusion of a fractional order term may improve the properties of the PR controller configurations even further. However, attention must be paid to the way the fractional exponent value is changed, as it may also lead to instabilities. Third, the interlinked relation among the fractional exponent, the AC grid weakness and the complementary feedback branch inductance is revealed for each fractional order PR configuration, and the corresponding tuning guidance is given. Moreover, a sensitivity analysis considering the AC filter inductance size is carried out and the tuning criteria are reformulated for each FPR controller.

Hence, the core of this paper is to clarify the role of the fractional exponent in an FPR-controlled VSC embedded in an AC grid environment, for given proportional and integral parameters. In this way, the differential impact of the fractional exponent on the stability can be addressed for diverse PR controller topologies. Besides, due to the inherent growing complexity in the electrical power systems nowadays, resonances may appear among electrically close systems. Therefore, it is important to analyse the differential impact of extra controller degrees of freedom provided by diverse PR topologies. For this purpose, the values for proportional and integral parameters are selected so that the integer order PR topology is stable but is also close to the stability limit.

The paper is organised as follows. In Section II, a comparative analysis is achieved among the different integer order PR topologies according to frequency response. In Section III, the methodology for tuning the fractional exponent is presented. In Section IV, the selected approximation for s^{α} is described. In Section V, the FPR controller functions are built based on the selected rational approximation and afterwards, an eigenvalue trajectory analysis is made for each FPR controller. Therefore, a first range of values for α are deduced for each fractional order PR controller in closed-loop configuration, in order to ensure the stability. In Section VI, the previous eigenvalue analysis is first verified for a VSC in an specific weak AC grid application. A more refined range of values for s^{α} in each fractional order PR topology is obtained and considerations regarding to the AC grid short-circuit ratio (SCR) values, other control parameters and AC filter inductance are examined. In Section VII, the conclusions are presented.

II. COMPARATIVE ANALYSIS OF INTEGER ORDER RESONANT CONTROL STRUCTURES

In this Section, different selected types of integer order PR control architectures are compared according to their frequency behaviour. The impact of the integral and proportional control parameters of PR controllers on the bode diagram and their extension for inverse sequence and for harmonic compensation have been sufficiently covered in the literature, as shown in [3], [18]–[20]. This Section is intended to serve the purpose of clarifying the main differences among PR controller types before including in them the fractional order terms.

In these comparisons, the baseline reference topology is the ideal PR controller, whose transfer function, G_{IPR}^{OL}, in the

Laplace domain is indicated in (1)

$$G_{IPR}^{OL} = k_p + k_i \frac{s}{s^2 + \omega^2} \tag{1}$$

As indicated in the introduction, different modifications of the ideal PR transfer function are found in the literature. One of them is the non-ideal PR topology, whose transfer function, G_{NIPR}^{OL}, is shown in (2), where a first order damping term, $2\omega_c s$, has been added in the denominator.

$$G_{NIPR}^{OL} = k_p + k_i \frac{\omega_c s}{s^2 + 2\omega_c s + \omega^2} \tag{2}$$

Another variation of the ideal PR architecture is the complex-vector PR topology, whose transfer function, G_{CVPR}^{OL}, is shown in (3), which includes a second order term in the numerator.

$$G_{CVPR}^{OL} = \frac{k_p s^2 + k_i s}{s^2 + \omega^2} \tag{3}$$

In (1)-(3), k_p and k_i are the proportional and integral control parameters, ω is the resonance frequency and ω_c is the damping frequency, in rad/s. The open-loop transfer functions presented in (1)-(3) are transformed into closed-loop structures by following (4) and taking into account the resistive and inductive components of the filter, R_f and L_f, respectively.

$$G^{CL} = \frac{\frac{G^{OL}}{L_f s + R_f}}{1 + \frac{G^{OL}}{L_f s + R_f}} \tag{4}$$

Being superscript ^{OL} the open-loop transfer function and superscript ^{CL} the closed-loop transfer function in (4).

The derived closed-loop transfer functions from the open-loop PR control structures are compared in terms of their frequency behaviour in Fig.1, for $\omega = 314.159$ rad/s, $\omega_c = 5$ rad/s, $R_f = 0.1$ Ohm, $L_f = 1.8$ mH, $k_p = 11.3$ and $k_i = 628$, as implemented in [18]. For this purpose, their bode magnitude and phase diagrams are presented for the frequency range corresponding to direct sequence, i.e. in the surroundings of positive resonant frequency. As shown in Fig.1,

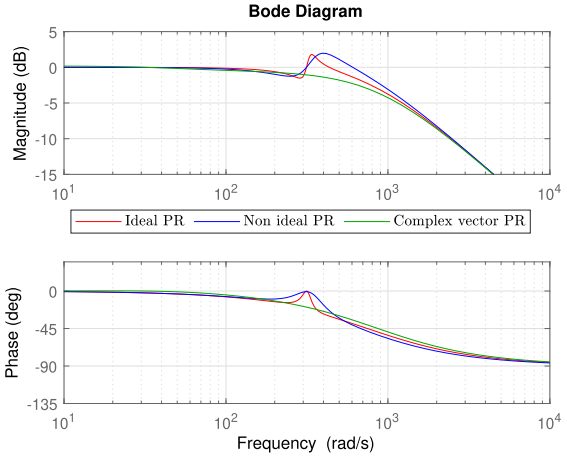

FIGURE 1. Bode magnitude and phase diagrams of closed-loop transfer functions of ideal, non-ideal and complex-vector PR controllers.

at the resonance frequency, 314.159 rad/s, the ideal and non-ideal PR controllers present a slope in the magnitude diagram and a peak at the phase diagram. The observed slope and peak are smoothed in the non-ideal PR topology in comparison with the ideal PR controller, and this depends on the size of the first order damping term, $2\omega_c$s. In turn, the complex-vector PR topology does not present a slope or any phase peak in the magnitude and diagram nor a peak in the phase diagram. The degree of the slope around the resonance frequency indicates the dependency of the controller architecture on frequency fluctuations. The comparison in Fig. 1 is supported by the analysis in [18].

As for those PR control architectures derived from the inclusion of feedback complementary branches, in Fig. 2 the different topologies are presented one by one, PR, PRXF, PRXC and PRX2, based on the analysis conducted in [20].

It can be noted that both PRXF and PRX2 configurations contain a feedback $j\omega L_b$ branch that is summed at the output of the controller, whereas PR and PRXC not. In turn, PRXC and PRX2 topologies present complex imaginary terms in their denominators.

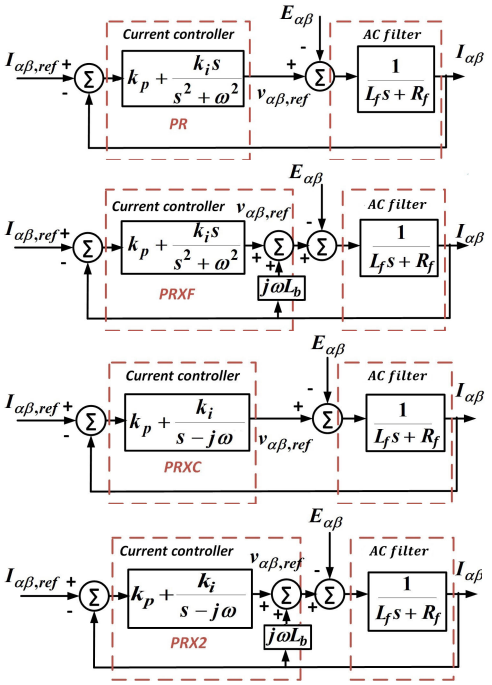

FIGURE 2. PR architectures according to the inclusion of feedback complementary branches: PR, PRXF, PRXC and PRXC.

The bode magnitude and phase diagrams of PR, PRXF, PRXC and PRX2 closed-loop PR controllers is shown in Fig.3, for which the AC filter parameters are set to $L_f = 1.8$ mH, $R_f = 0.1$ Ohm, while $L_b = 1.8$ mH, $k_p = 3.3$ and $k_i = 628$.

The bode responses of closed-loop ideal PR and PRXC structures shown in Fig. 3 present the maximum slope at the resonant frequency in direct sequence, +314.159 rad/s, compared to PRXF and PRX2 topologies. Nevertheless,

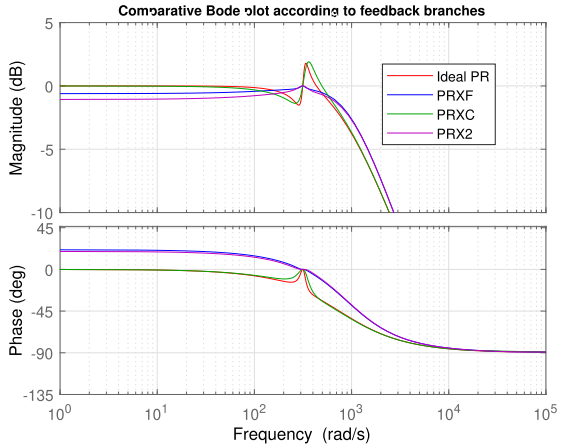

FIGURE 3. Bode magnitude and phase diagrams of closed-loop transfer functions of ideal PR, PRXF, PRXC and PRX2 controllers.

the PRXC controller also achieves a slight reduction of the gain slope with respect to ideal PR controller. With regard to bode phase diagrams, the ideal PR and PRXC controllers present an observable phase peak at resonant frequency, whereas PRXF and PRX2 just present a negligible variation. Even so, the PRXC scheme smoothes the phase peak at the resonant frequency with respect to the ideal PR scheme.

The comparison extracted from the bode diagrams in Fig. 3 reflects the benefits, on the one hand, of adding a $j\omega L_b$ feedback branch in terms of reducing their sensitivity to frequency changes, as seen in the bode magnitude diagram of PRXF and PRX2 schemes. On the other hand, the inclusion of imaginary terms in the denominators of their transfer functions, as seen in PRXC and PRX2 schemes, also achieves a slight reduction of the gain slope at the resonant frequency, in comparison with the ideal PR topology.

In order to summarise, the complex-vector, PRXF and PRX2 schemes are those that mostly reduce the dependency of a PR controller to frequency changes, though the non-ideal and PRXC schemes still achieve a small reduction.

III. METHODOLOGY FOR TUNING FRACTIONAL ORDER RESONANT CONTROLLERS

In this Section, a novel methodology for the tuning of FPR control structures is described by means of the diagram presented in Fig. 4.

The steps followed by the diagram in Fig. 4 are hereafter detailed one by one. First, a proper rational approximation for the s^α term is selected and, as a result, each s^α with fractional exponent, α, can be represented by an appropiate rational polynomial function composed by integer order terms. The resulting function is dependent on α and the chosen degree of polynomial.

Based on this approximation, the integer order PR controllers presented in Section II can be transformed into fractional order PR controllers. Once these FPR controllers have been built, an eigenvalue analysis of the closed-loop form of

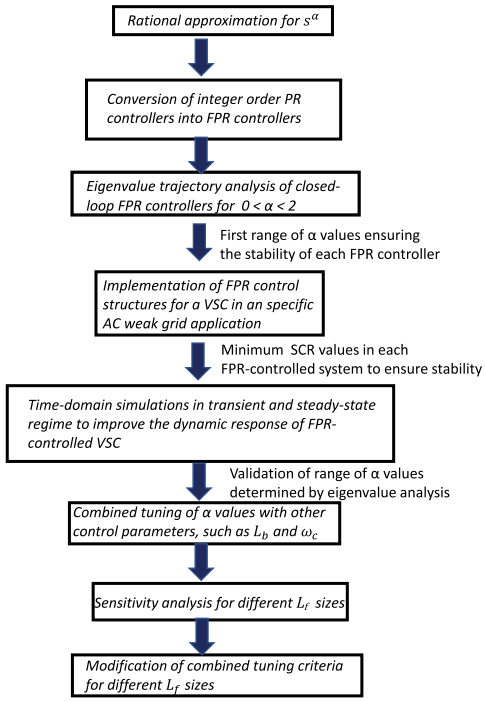

FIGURE 4. Diagram of the proposed novel methodology.

the FPR controllers is carried out to obtain a first range of fractional exponents that ensure stability.

In order to validate the corresponding α values in a weak AC grid context, as well as to test its impact on the transient dynamic behaviour, each FPR controller is implemented in a specific application consisting in an FPR-controlled VSC connected to a weak AC grid. In order to define the scenarios, a minimum SCR value of the weak AC grid is determined for each FPR-controlled VSC.

Once the scenarios for each FPR-controlled system have been defined, time-domain simulations are executed in order to test the dynamic transient and steady-state responses under perturbations in grid current setpoints. The responses will be evaluated in terms of oscillation peak and oscillation amplitude, settling time, tracking capabilities, and the possibility of improvement by tuning α in combination with other control parameters such as ω_c or L_b.

After carrying out the time-domain simulations, criteria for tuning FPR control structures in combination with other control parameters, such as ω_c or L_b are extracted for each FPR control structure.

In the end, the methodology also considers the reformulation for different AC filter sizes, L_f, and thus, slight modifications of tuning criteria for each FPR controller are proposed based on a new L_f size.

IV. THE INCLUSION OF FRACTIONAL ORDER TERM IN INTEGER ORDER PR CONTROL STRUCTURES

This Section is intended to give a brief overview on fractional calculus and describe the rational approximation used to

represent the fractional order s^α term. Based on this approximation, the FPR transfer functions corresponding to the PR schemes showed in Section II can be computed. The rational approximation of a fractional order term obtains transfer functions composed by integer order polynomial terms and thus it is possible to work as it was an integer order system, as authors in [24], [25] considered. Otherwise, Matignon's theorem implications should be applied, as the authors in [36], [37] did.

In [21]–[25] several continuous approximations to represent fractional order s^α terms are described. Among them, general fraction expansion, Carlson's and Matsuda's methods use continuous fraction expansion and interpolation techniques. In turn, Oustaloup's and Chareff's methods use curve fitting and identification techniques. Apart from these, in [21] several discrete approximatons to represent fractional order s^α terms are also listed, among which those using numerical integration and power series or continuous fraction expansion can be found. In [35] a systematic procedure is presented to give a rational approximation to s^α, for $0 < \alpha < 1$, based on continued fraction expansion technique.

The procedure presented on [35] is summarised as follows. A set of polynomial coefficients must be calculated according to the selected order type of the approximation and the value of fractional exponent, α. For 1^{st}, 2^{nd}, 3^{rd} and 4^{th} order types, the author in [35] gives the rational expression for s^α in (5), (6), (7) and (8), respectively.

$$s^\alpha_{1^{st}} \approx \frac{p_{10}s + p_{11}}{q_{10}s + q_{11}} \tag{5}$$

$$s^\alpha_{2^{nd}} \approx \frac{p_{20}s^2 + p_{21}s + p_{22}}{q_{20}s^2 + q_{21}s + q_{22}} \tag{6}$$

$$s^\alpha_{3^{rd}} \approx \frac{p_{30}s^3 + p_{31}s^2 + p_{32}s + p_{33}}{q_{30}s^3 + q_{31}s^2 + q_{32}s + q_{q33}} \tag{7}$$

$$s^\alpha_{4^{th}} \approx \frac{p_{40}s^4 + p_{41}s^3 + p_{42}s^2 + p_{43}s + p_{44}}{q_{40}s^4 + q_{41}s^3 + q_{42}s^2 + q_{q43}s + q_{44}} \tag{8}$$

The polynomial coefficients in (5), (6), (7) and (8) are calculated as a function of the fractional exponent, α. The corresponding polynomial coefficients are defined in (9), (10), (11) and (12), respectively.

$$\begin{aligned} p_{10}(\alpha) &= q_{11}(\alpha) = (\alpha + 1) \\ p_{11}(\alpha) &= q_{10}(\alpha) = -(\alpha - 1) \end{aligned} \tag{9}$$

$$\begin{aligned} p_{20}(\alpha) &= q_{22}(\alpha) = \prod_{i=1}^{2}(\alpha + i) \\ p_{21}(\alpha) &= q_{21}(\alpha) = -2 \prod_{i=-2,2} (\alpha - i) \\ p_{22}(\alpha) &= q_{20}(\alpha) = \prod_{i=1}^{2}(\alpha - i) \\ p_{30}(\alpha) &= q_{33}(\alpha) = \prod_{i=1}^{3}(\alpha + i) \end{aligned} \tag{10}$$

$$\begin{aligned} p_{31}(\alpha) &= q_{32}(\alpha) = -3(\alpha - 3)\prod_{i=2}^{3}(\alpha + i) \\ p_{32}(\alpha) &= q_{31}(\alpha) = 3(\alpha + 3)\prod_{i=2}^{3}(\alpha - i) \\ p_{33}(\alpha) &= q_{30}(\alpha) = -\prod_{i=1}^{3}(\alpha - i) \end{aligned} \tag{11}$$

$$\begin{aligned} p_{40}(\alpha) &= q_{44}(\alpha) = \prod_{i=1}^{4}(\alpha + i) \\ p_{41}(\alpha) &= q_{43}(\alpha) = -4\prod_{i=3}^{4}(\alpha - i)\prod_{i=3}^{4}(\alpha + i) \\ p_{42}(\alpha) &= q_{42}(\alpha) = 6\prod_{i=3}^{4}(\alpha - i)\prod_{i=3}^{4}(\alpha + i) \\ p_{43}(\alpha) &= q_{41}(\alpha) = -4\prod_{i=3}^{4}(\alpha - i) \\ p_{44}(\alpha) &= q_{40}(\alpha) = \prod_{i=1}^{4}(\alpha - i) \end{aligned} \tag{12}$$

The rational approximation of s^α has been chosen in the 4^{th} order type, since the error converges more rapidly than with lower order types, as reported in [18]. In order to work with fractional exponents greater than 1, an integer order term can be multiplied by the selected rational approximation for s^α.

V. EIGENVALUE TRAJECTORY ANALYSIS

Once the rational approximation for s^α has been defined, the open-loop FPR control structures can be computed according to Section IV. In this Section, an eigenvalue trajectory analysis is presented in order to clarify the effect of varying the fractional exponent, α, in each FPR control structure. The control parameter values for each FPR closed-loop system can be consulted in Appendix A.

A. FRACTIONAL ORDER IDEAL PROPORTIONAL RESONANT CONTROLLER (FIPR)

The open-loop FIPR transfer function, G^{OL}_{FIPR}, is indicated in (13).

$$G^{OL}_{FIPR} = k_p + k_i \frac{s^\alpha}{s^2 + \omega^2} \tag{13}$$

The G^{OL}_{FIPR} open-loop transfer function is included in the closed-loop structure shown in (4) and the corresponding closed-loop transfer function, G^{CL}_{FIPR}, is obtained.

The eigenvalue trajectories for G^{CL}_{FIPR} are shown in Fig. 5, for α ranging from 0 to 2.

The colorbar in Fig. 5 links the α value with the color code observed in the trajectories of eigenvalues. In the zoomed area of Fig. 5, it can be observed that the trajectories for $\alpha < 1$ (dark and light blue-green) lay in the right side of the complex plane and therefore indicate unstable behaviour

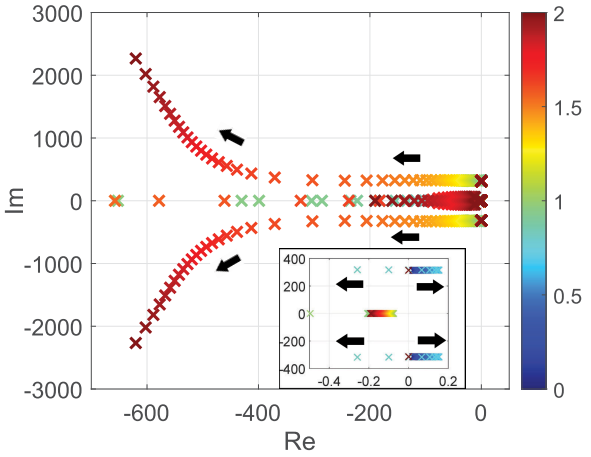

FIGURE 5. Eigenvalue trajectory analysis for G^{CL}_{FIPR}.

in the closed-loop control structure. Instead, for $\alpha \geq 1$ the eigenvalues move to the left half-plane and the stability is recovered again once they cross the imaginary axis, when $\alpha = 1$.

B. FRACTIONAL ORDER NON-IDEAL PROPORTIONAL RESONANT CONTROLLER (FNIPR)

The open-loop FNIPR transfer function, G^{OL}_{FNIPR}, is indicated in (14).

$$G^{OL}_{FNIPR} = k_p + k_i \frac{\omega_c s^\alpha}{s^2 + 2\omega_c s + \omega^2} \tag{14}$$

The G^{OL}_{FNIPR} open-loop transfer function is included in the closed-loop structure shown in (4) and the corresponding closed-loop transfer function G^{CL}_{FNIPR} is obtained.

The eigenvalue trajectories for G^{CL}_{FNIPR} are shown in Fig. 6, for α ranging from 0 to 2.

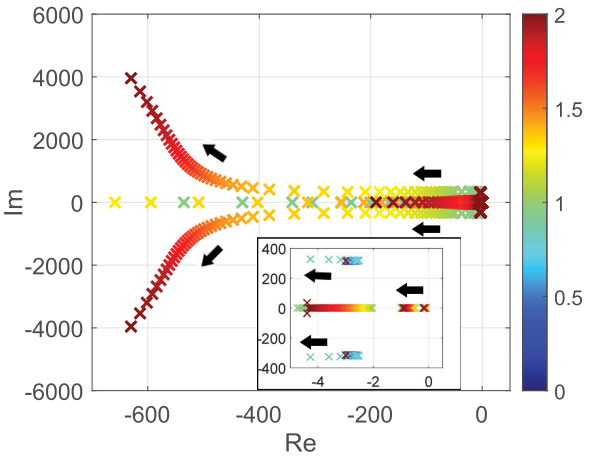

FIGURE 6. Eigenvalue trajectory analysis for G^{CL}_{FNIPR}.

As seen in Fig. 6, the inclusion of a first order damping term encloses the complete set of trajectories in the left half-plane, with respect to the previous FIPR controller. Therefore, no instability issues are found for this configuration and the assigned value of damping frequency, ω_c. For greater ω_c values, the critical eigenvalues that were unstable in FIPR diagram are further moved to the left and therefore, the stability margin is increased.

C. FRACTIONAL ORDER COMPLEX VECTOR PROPORTIONAL RESONANT CONTROLLER (FCVPR)

The open-loop FCVPR transfer function, G^{OL}_{FCVPR}, is indicated in (15).

$$G^{OL}_{FCVPR} = \frac{k_p s^2 + k_i s^\alpha}{s^2 + \omega^2} \tag{15}$$

The G^{OL}_{FCVPR} open-loop transfer function is included in the closed-loop structure shown in (4) and the corresponding closed-loop transfer function G^{CL}_{FCVPR} is obtained.

The eigenvalue trajectories for G^{CL}_{FCVPR} are shown in Fig. 7, for α ranging from 0 to 2.

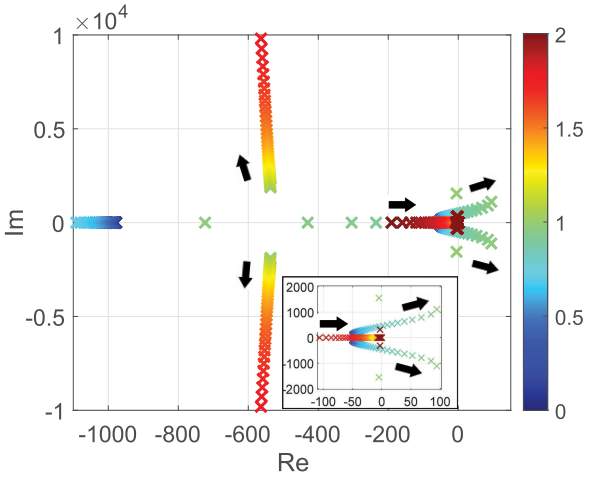

FIGURE 7. Eigenvalue trajectory analysis for G^{CL}_{FCVPR}.

The trajectories in Fig. 7 show that, while for $\alpha \leq 1$ the eigenvalues remain in the stable area, for $1 < \alpha < 1.25$ they cross the imaginary axis and reach the unstable side of the complex plane. The stability is eventually recovered for $\alpha \geq 1.25$.

D. FRACTIONAL ORDER PROPORTIONAL RESONANT CONTROLLER WITH XFEEDBACK BRANCH (FPRXF)

The open-loop FPRXF transfer function, G^{OL}_{FPRXF}, is indicated in (16).

$$G^{OL}_{FPRXF} = k_p + k_i \frac{s^\alpha}{s^2 + \omega^2} \tag{16}$$

The G^{OL}_{FPRXF} open-loop transfer function replaces the PRXF current controller in Fig.2, and by including the $j\omega L_b$ feedback branch, the corresponding closed-loop transfer function G^{CL}_{FPRXF} is obtained.

The eigenvalue trajectories for G^{CL}_{FPRXF} are shown in Fig. 8, for α ranging from 0 to 2.

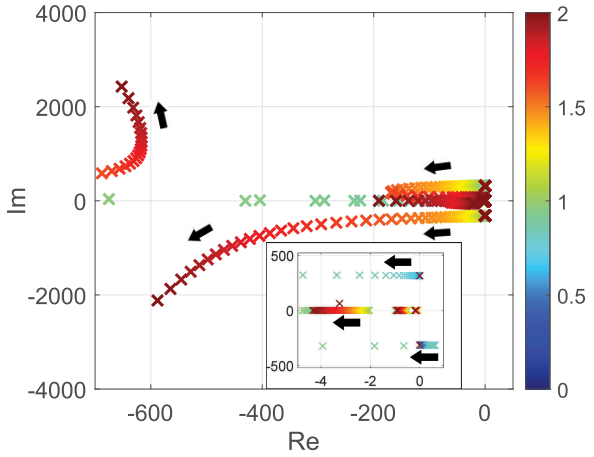

FIGURE 8. Eigenvalue trajectory analysis for G^{CL}_{FPRXF}.

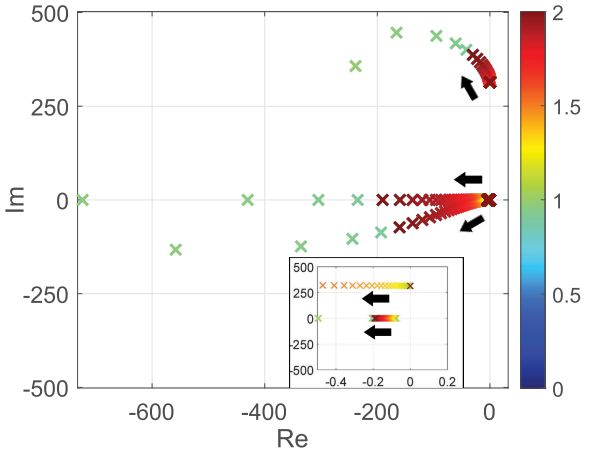

FIGURE 9. Eigenvalue trajectory analysis for G^{CL}_{FPRXC}.

In Fig. 8 the trajectories of eigenvalues are not symmetrical with respect to the real axis due to the inclusion of the $j\omega L_b$ feedback branch. Since the G^{OL}_{FPRXF} function is identical to the G^{OL}_{FIPR} function, the stability diagnostic for G^{CL}_{FPRXF} via eigenvalue trajectory is similar to the one obtained for G^{CL}_{FIPR}. In this sense, the eigenvalue trajectories covered by the range α<1 show an unstable behaviour, as they lay in the right half-plane. In contrast, for $\alpha \geq 1$, the system turns to be stable, as the trajectories lay in the left half-plane.

E. FRACTIONAL ORDER PROPORTIONAL RESONANT CONTROLLER WITH XControl BRANCH (FPRXC)

The open-loop FPRXC transfer function, G^{OL}_{FPRXC}, is indicated in (17).

$$G^{OL}_{FPRXC} = k_p + k_i \frac{s^\alpha}{s - j\omega} \tag{17}$$

The G^{OL}_{FPRXC} open-loop transfer function is included in the closed-loop structure shown in (4) and the corresponding closed-loop transfer function G^{CL}_{FPRXC} is obtained.

The eigenvalue trajectories for G^{CL}_{FPRXC} are shown in Fig. 9, for α ranging from 0 to 2. In Fig. 9 the trajectories of eigenvalues are not symmetrical with respect to the real axis due to the presence of the imaginary term, $j\omega$, in the open-loop function, G^{OL}_{FPRXC}. The trajectories in Fig. 9 are commpletely enclosed in the left half-plane and therefore, the system is stable for the entire range $0 < \alpha < 2$.

F. FRACTIONAL ORDER PROPORTIONAL RESONANT CONTROLLER WITH X_2 BRANCH (FPRX2)

The open-loop FPRX2 transfer function, G^{OL}_{FPRX2}, is indicated in (18).

$$G^{OL}_{FPRX2} = k_p + k_i \frac{s^\alpha}{s - j\omega} \tag{18}$$

The G^{OL}_{FPRX2} open-loop transfer function replaces the PRX2 current controller in Fig. 2, and by including the $j\omega L_b$ feedback branch, the corresponding closed-loop transfer function G^{CL}_{FPRX2} is obtained.

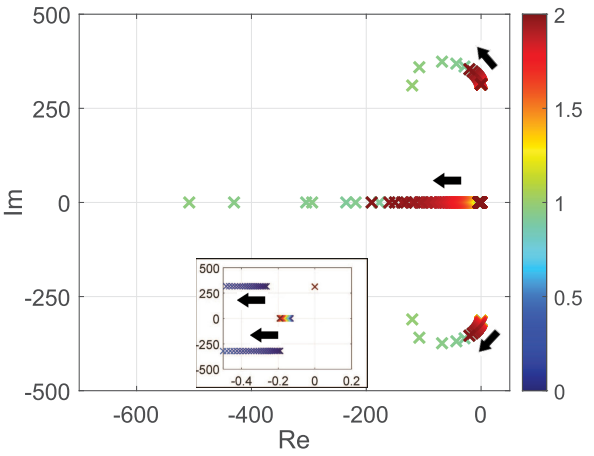

FIGURE 10. Eigenvalue trajectory analysis for G^{CL}_{FPRX2}.

The eigenvalue trajectories for G^{CL}_{FPRX2} are shown in Fig. 10, for α ranging from 0 to 2.

In Fig. 10 the trajectories of eigenvalues are symmetrical with respect to the real axis due to, on the one hand, the presence of the imaginary term, $j\omega$, in the open-loop function, G^{OL}_{FPRXC}, and on the other hand, the inclusion of the $j\omega L_b$ feedback branch in the closed-loop configuration. Apart from this, the trajectories in Fig. 10 are commpletely enclosed in the left half-plane and therefore, the system is stable for the entire range $0 < \alpha < 2$.

G. TUNING IMPLICATIONS

According to the analysis carried out along this Section, several first tuning implications for each type of FPR topology can be extracted.

- Both FIPR and FPRXF controllers are stable for $1 \leq \alpha < 2$ and unstable for $\alpha < 1$. With regard to FPRXF controller, the presence of the $j\omega L_b$ feedback branch in the closed-loop arrangement makes the eigenvalue trajectories asymmetrical with respect to real axis.

- The FNIPR controller is stable for the complete range of $0 < \alpha \leq 2$. The presence of the damping frequency, ω_c, has stabilised the unstable eigenvalues observed in the FIPR case for $0 < \alpha < 1$. For greater ω_c values, the critical eigenvalues will move further to the left side of the plane and will increase the stability margin. For lower ω_c values, the critical eigenvalues will be closer to the imaginary axis and the stability margin will be reduced.
- As for FCVPR controller, for $\alpha \leq 1$ the system is stable, but when $1 < \alpha < 1.25$ is unstable. Eventually, it recovers stability for $\alpha \geq 1.25$.
- With regard to FPRXC and PRX2 controllers, the trajectories of eigenvalues are kept inside the left half-plane for α ranging from 0 to 2, and therefore both controllers maintain the stability of the system for the tested α range. Besides, in FPRXC the presence of an imaginary term in the open-loop transfer function makes the eigenvalue trajectories asymmetrical with respect to the real axis. In the case of PRX2 function, the presence of both $j\omega L_b$ feedback branch and the imaginary term in the open-loop function, makes the trajectories symmetrical with respect to the real axis.

VI. SIMULATIONS IN TRANSIENT REGIME FOR A VSC CONNECTED TO A WEAK AC GRID

The eigenvalue analysis developed in Section V has provided a first estimation of the ranges for the fractional index that ensure the stability of each FPR system. However, other critical variables for stability, such as the weakness of the AC grid to which the FPR-controlled VSC is connected, have not been included in the analysis. Therefore, this section is intended to consider the influence of a weak AC grid connection in the analysis and, eventually, validate it via time-domain simulations in an specific model application.

A. DESCRIPTION OF THE APPLICATION

The model application consists in a FPR-controlled VSC connected to a weak AC grid with adjustable SCR values and is implemented in Matlab-Simulink. It consists of a set of MMCs governed by the different FPR control structures, where each of them is connected to a weak AC grid with adjustable SCR. Each MMC is fed by a constant voltage source, which models an HVDC link connection in steady-state operation with high content of renewables.

In Fig. 11, the general schematic for such model application is presented, where the constant voltage source is represented by V_{DC}.

Besides, the AC line is modelled by means of a Π-equivalent section and the AC grid by its Thévenin equivalent. The AC grid resistance and inductance, R_{AC} and L_{AC}, are parameterised as a function of the AC grid apparent power $S_{AC,grid}$, which is adjustable to simulate different weak AC grid cases. These weak AC grid cases are obtained for different values of the short-circuit ratio at the point of common coupling (SCR_{PCC}) and its corresponding apparent power, S_{PCC}. The SCR_{PCC}, S_{PCC}, $S_{AC,grid}$, R_{AC} and L_{AC} values for each weak AC grid scenario are presented in Appendix B.

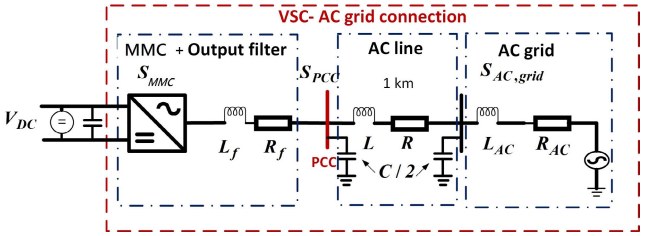

FIGURE 11. Application case: MMC connected to a weak AC grid with adjustable short-circuit ratio (SCR).

TABLE 1. Parameters for the application case.

Parameter	Description	Value
V_{AC}	AC voltage level	275 kV
V_{DC}	DC voltage level	640 kV
L_f	AC filter inductance	18 mH
R_f	AC filter resistance	0.1 Ω
L	AC line inductance per kilometer	0.4 mH/km
R	AC line resistance per kilometer	0.125 Ω/km
C	AC line capacitance per kilometer	0.22 μF/km
l	Length of the AC line	1 km
S_{MMC}	Apparent power of MMC	560 MVA
N	Total number of submodules per MMC arm	200
C_{sm}	Capacitance of an MMC submodule	20 μF
R_{arm}	MMC arm resistance	1 Ω
L_{arm}	MMC arm inductance	18 mH

In Table 1, the main physical parameters of the system presented in Fig.11 are listed.

The MMC presents the arrangement indicated in Fig. 12. The MMC has three legs, one per phase, and each leg has an upper and a lower arm. The set of submodules (SM), N, are distributed homogeneously along each upper and lower arm. In order to control the MMC, the insertion indices are used to calculate the number of submodules that are inserted in an arm. In this sense, an insertion index of 1 means that all submodules within that arm are inserted, and therefore the arm voltage reaches its maximum value, V_{DC}. In contrast,

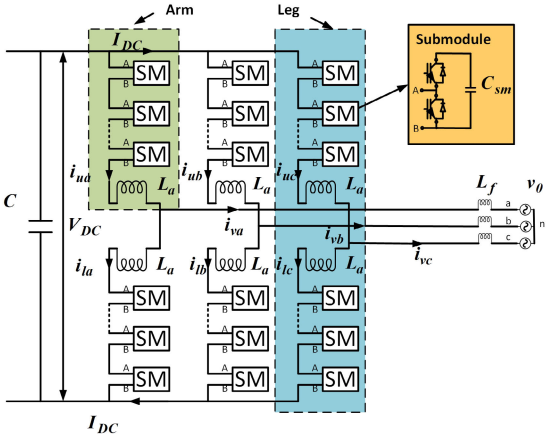

FIGURE 12. Detailed scheme of MMC.

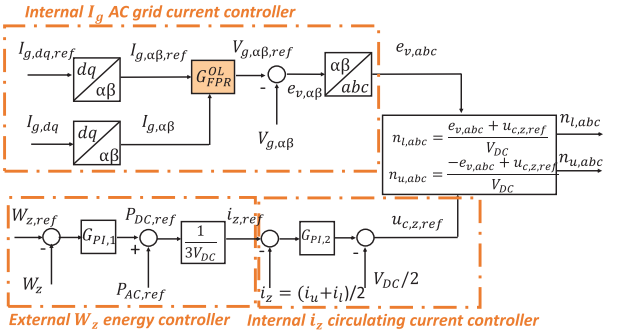

FIGURE 13. MMC global control scheme.

if the insertion index is zero, no submodule is inserted in that arm and the arm voltage reaches zero.

The FPR current control function has been integrated in the global control structure as indicated in Fig. 13. The objective of this global control is to obtain the insertion indices, $n_{l,abc}$ and $n_{u,abc}$, which are calculated according to the expressions showed in Fig. 13, and depend on two contributions, $e_{v,abc}$ and $u_{c,z,ref}$. These two magnitudes come fom the grid and circulating current control schemes, respectively.

In Fig. 13, the G^{OL}_{FPR} block (either G^{OL}_{FIPR}, G^{OL}_{FNIPR}, G^{OL}_{FCVPR}, G^{OL}_{FPRXF}, G^{OL}_{FPRXC} or G^{OL}_{FPRX2}) is the open-loop FPR control structure, which is highlighted in color and is included in the internal grid current controller. For this purpose, the incoming grid and reference currents in dq coordinates, $I_{g,dq}$ and $I_{g,dq,ref}$, are converted into $\alpha\beta$ coordinates to adequate the inputs for the FPR current controller. The outputs of the FPR controller are the $\alpha\beta$ voltage references, $V_{g,\alpha\beta,ref}$, which are substracted to $\alpha\beta$ grid voltages and as a result, the error $e_{v,\alpha\beta,ref}$ is obtained. This magnitude is transformed into abc frame and turns to be the $e_{v,abc}$ contribution.

Besides, the other contribution for the calculation of the insertion indices is $u_{c,z,ref}$, and it is computed by means of the circulating current controller. This is composed by an external energy controller, which is responsible for the generation of the circulating current reference, $i_{z,ref}$. The $i_{z,ref}$ signal is obtained by integrating the error between the MMC energy reference, $W_{z,ref}$, and actual MMC energy, W_z in z component. The generated $i_{z,ref}$ current reference is compared by the actual circulating current, i_z, and the error integrated by a PI function. The final output is summed to $V_{DC}/2$ and, eventually, the $u_{c,z,ref}$ contribution from the circulating current controller is obtained.

With these two contributions, $e_{v,abc}$ and $u_{c,z,ref}$, the insertion indices for the lower and upper arm, $n_{l,abc}$ and $n_{u,abc}$, are calculated in abc coordinates and directly injected to the MMC.

The parameters of the remaining control blocks in Fig. 13, other than the FPR function, are detailed in the Appendix C.

B. ANALYSIS OF DYNAMIC RESPONSE VIA TIME-DOMAIN SIMULATIONS

In the model application described in Subsection VI.A, the different FPR control structures are tested one by one for a range of varying α, while several SCR values of the weak AC grid are considered. The resulting time-domain simulations in transient regime are hereafter presented for each FPR controller.

The complete set of scenarios is enclosed in Table 2.

TABLE 2. Baseline scenarios for time-domain simulations in transient regime.

FPR	k_p	k_i	$S_{AC,grid}$ (MVA)	SCR_{PCC}
FIPR	1.5	50	800	1.47
FNIPR	1.5	50	800	1.47
FCVPR	1.5	5000	1300	2.34
FPRXF	1.5	50	800	1.47
FPRXC	11	628	800	1.47
FPRX2	11	628	800	1.47

The baseline scenario for FCVPR controller is set with a higher SCR_{PCC} value, due to instability issues previously reported in [18] and also due to the results from the eigenvalue analysis in Section V, compared to other FPR controllers. Apart from these values, a common value of resonant frequency $\omega = 314.159$ rad/s is considered, as well as the AC filter values, $R_f = 0.1\ \Omega$ and $L_f = 18$ mH. The FPR schemes that have a complementary feedback branch, i.e. FPRXF and FPRX2, have its feedback branch inductance tuned at $L_b = 0.4$ mH. By considering the data listed in Table 2, for each FPR-controlled VSC, the dq current setpoints in Fig. 14 are injected as inputs to the FPR controller.

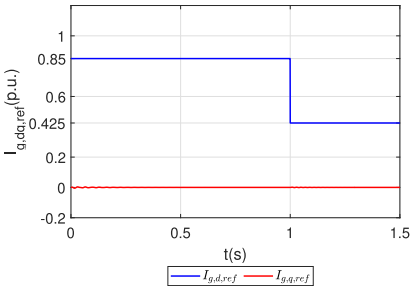

FIGURE 14. Current setpoints.

From now on, the behaviour of each FPR-controlled system under these inputs is analysed via time-domain simulations. The impact of each FPR control parameters on the transient and steady-state behaviour is analysed afterwards for each FPR control function.

1) FIPR-CONTROLLED VSC CONNECTED TO A WEAK AC GRID

Since the results from eigenvalue analysis for FIPR control structure pointed out $\alpha = 1$ as the inflexion point below which the system was unstable and above which the system was stable, the time-domain simulations have also been separated for those $0 < \alpha < 1$ and $1 \leq \alpha \leq 2$. In Fig. 15, the transient grid current responses in p.u., $I_{g,d}$ and $I_{g,q}$, are shown for different α values belonging to $0 < \alpha \leq 1$.

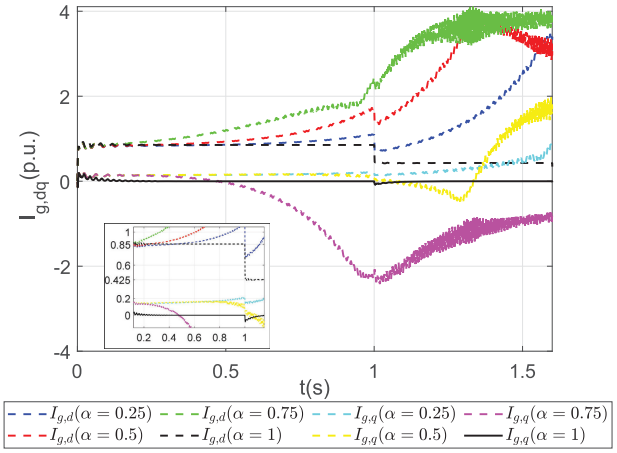

FIGURE 15. Simulation of FIPR in transient regime for $0 < \alpha \leq 1$.

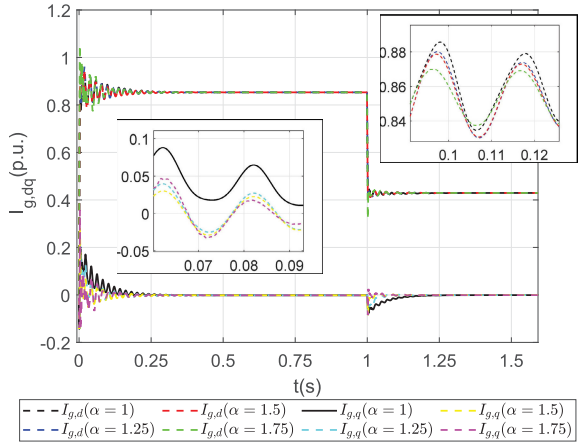

FIGURE 16. Simulation of FIPR in transient regime for $1 \leq \alpha < 2$.

In Fig. 15, it can be seen that those currents associated to $\alpha = 0.25$, $\alpha = 0.5$ and $\alpha = 0.75$, diverge from their respective set-points, $I_{g,d,ref}$ and $I_{g,q,ref}$, respectively, and are unstable, confirming the previous eigenvalue analysis and it is verified when embedded in a weak AC grid. In contrast, the current signals corresponding to $\alpha = 1$ are both stable and converge to the current set-points $I_{g,d,ref}$ and $I_{g,q,ref}$.

The transient responses for those FIPR controlled systems with α belonging to $1 \leq \alpha < 2$, are presented in Fig. 16. These responses are, in turn, stable, as pinpointed previously in the eigenvalue analysis. Moreover, it can be seen in the zoomed areas that the increasing order of α reduces the oscillatory peaks of the transient responses, $I_{g,d}$ and $I_{g,q}$. Besides, the signals reach their setpoints $I_{g,d,ref}$ and $I_{g,q,ref}$ in the steady-state regime.

2) FNIPR-CONTROLLED VSC CONNECTED TO A WEAK AC GRID

The inclusion of a first order term, $2\omega_c$s, in the denominator contributes to stabilise the system, as reported in the eigenvalue analysis. Therefore, for $\omega_c = 5$rad/s, the FNIPR-controlled system response is stable, as seen in Fig. 17, for α

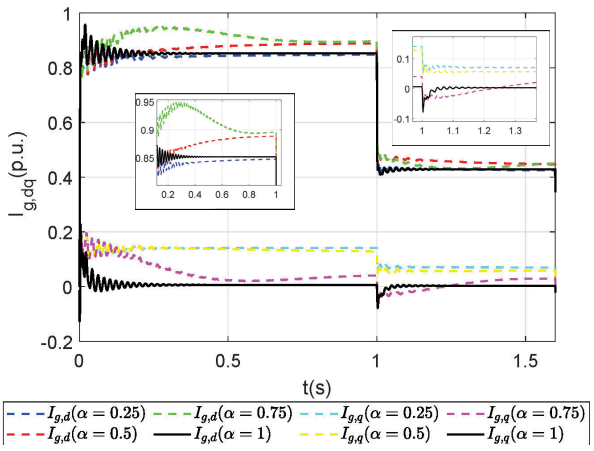

FIGURE 17. Simulation of FNIPR in transient regime for $0 < \alpha \leq 1$.

belonging to $0 < \alpha \leq 1$. However, the tracking capabilities are very poor, as seen in Fig. 17. Although the $I_{g,d}$ and $I_{g,q}$ signals converge to stable values, they do not match the $I_{g,d,ref}$ and $I_{g,q,ref}$ set-points. The reason behind this behaviour is the proximity to right half-plane of eigenvalue trajectories, for α belonging to $0 < \alpha \leq 1$.

Nevertheless, for α values belonging to $1 < \alpha < 2$, the $I_{g,d}$ and $I_{g,q}$ responses are stable and, besides, they converge to their setpoints, as seen in Fig. 18.

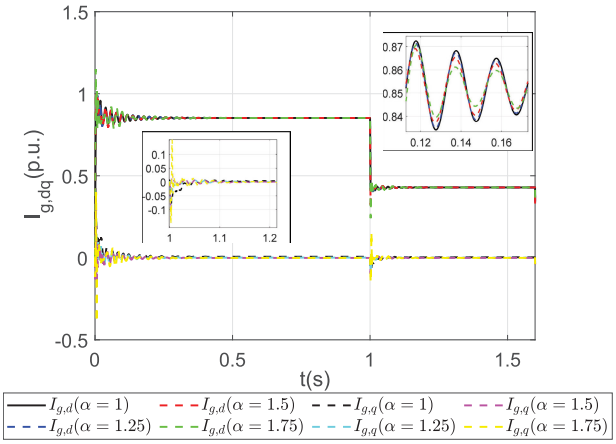

FIGURE 18. Simulation of FNIPR in transient regime for $1 \leq \alpha < 2$.

Therefore, as α is increased over 1, the tracking capabilities of the FNIPR controller improve and, in these cases, the oscillation peak in the signals is reduced with respect to the $\alpha = 1$ scenario.

3) FCVPR-CONTROLLED VSC CONNECTED TO A WEAK AC GRID

FCVPR controller also has an inflexion point regarding stability, which is $\alpha = 1$. Therefore, both $0 < \alpha \leq 1$ and $1 < \alpha < 2$ are examined separately. In the presence of a weak AC grid, the $I_{g,d}$ and $I_{g,q}$ responses corresponding to $0 < \alpha \leq 1$ are presented in Fig. 19.

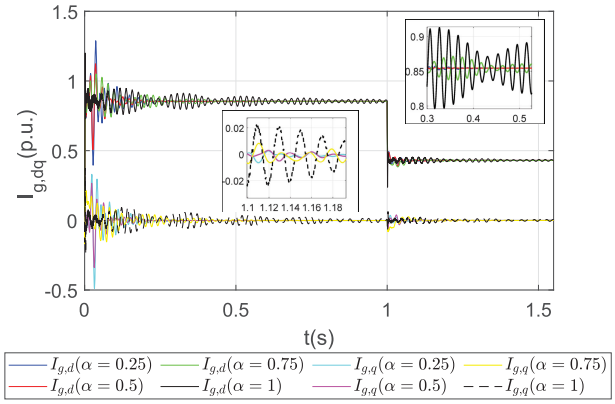

FIGURE 19. Simulation of FCVPR in transient regime for $0 < \alpha \leq 1$.

As observed in the zoomed areas of Fig. 19, the responses corresponding to $\alpha = 1$, are much worse in terms of dynamic behaviour than those with $\alpha < 1$. In fact, as far as α adopts lower values, the transient dynamic response improves.

However, for $1 < \alpha < 2$ the dyamic behaviour of $I_{g,d}$ and $I_{g,q}$ signals vary significantly, as seen in Fig. 20.

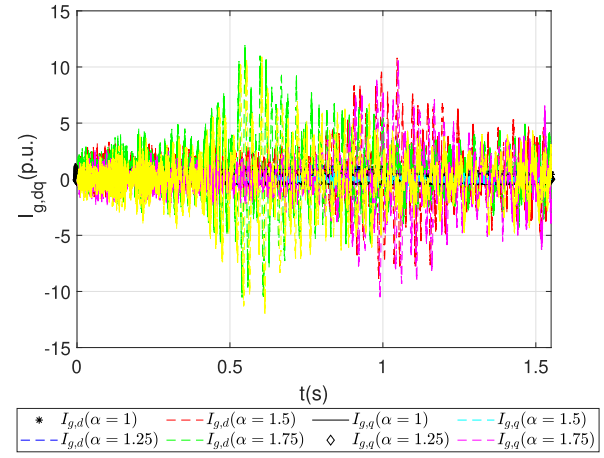

FIGURE 20. Simulation of FCVPR in transient regime for $1 \leq \alpha < 2$.

According to the theoretical eigenvalue analysis developed in Section V, for α values greater than 1.25 the system trajectories of FCVPR controller recovered the stability. However, no weak AC grid scenario was considered in the theoretical analysis, and therefore, the weak AC grid connection makes the system unstable for the entire range of $1 < \alpha < 2$.

4) FPRXF-CONTROLLED VSC CONNECTED TO A WEAK AC GRID

The results in Fig. 21 show the unstable responses of $I_{g,d}$ and $I_{g,q}$ for $0 < \alpha < 1$, as reported in the eigenvalue analysis.

Nevertheless, the $I_{g,d}$ and $I_{g,q}$ signals are stable when α belongs to $1 \leq \alpha < 2$, as showed in Fig. 22. In the stable cases, as with FNIPR andd FIPR-controlled systems, the oscillation peak is reduced, as far as α is increased above 1. Besides, not

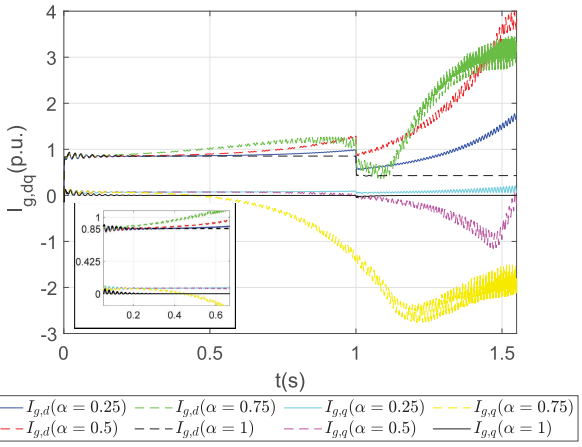

FIGURE 21. Simulation of FPRXF in transient regime for $0 < \alpha \leq 1$.

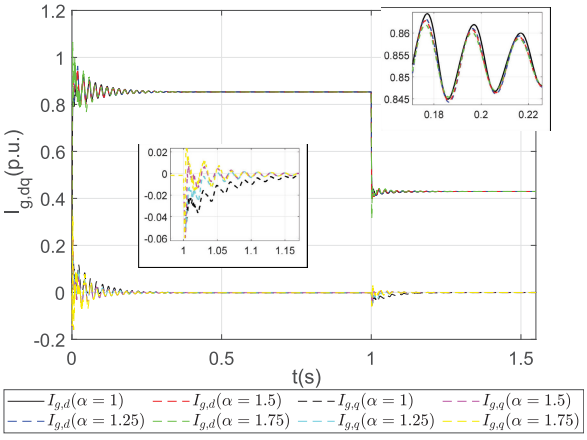

FIGURE 22. Simulation of FPRXF in transient regime for $1 \leq \alpha < 2$.

only the oscillation peak is reduced but also the oscillation amplitude.

The tracking capabilities for α belonging to $1 \leq \alpha < 2$ are adequate as the $I_{g,d}$ and $I_{g,q}$ signals converge to the corresponding setpoints.

5) FPRXC-CONTROLLED VSC CONNECTED TO A WEAK AC GRID

In the presence of a weak AC grid connection, the $I_{g,d}$ and $I_{g,q}$ responses of a FPRXC-controlled systm are stable as seen in Fig. 23, for the entire range of α belonging to $0 < \alpha < 2$. Each pair of $I_{g,d}$ and $I_{g,q}$ signals has negligible difference with other pairs within the α range tested, being almost coincident signals.

However, the tracking capabilities are very poor, as the $I_{g,d}$ and $I_{g,q}$ responses do not match the setpoints. This can be typically improved by changing the integral and or proportional parameters of the controller. However, in order to show the effect of adding a complementary feedback branch on improving the tracking capabilities of the FPRXC controller, no changes in k_p or k_i are explored, but in contrast,

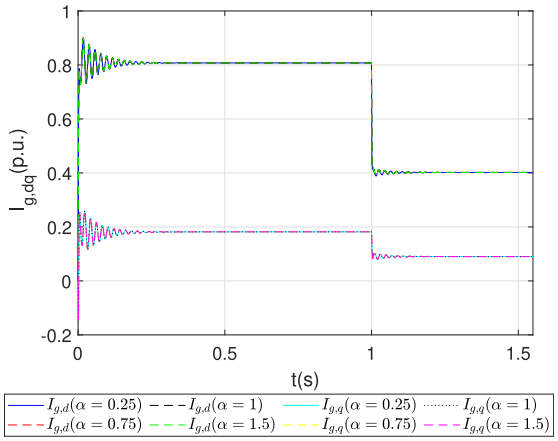

FIGURE 23. Simulation of FPRXC in transient regime for $0 < \alpha < 2$.

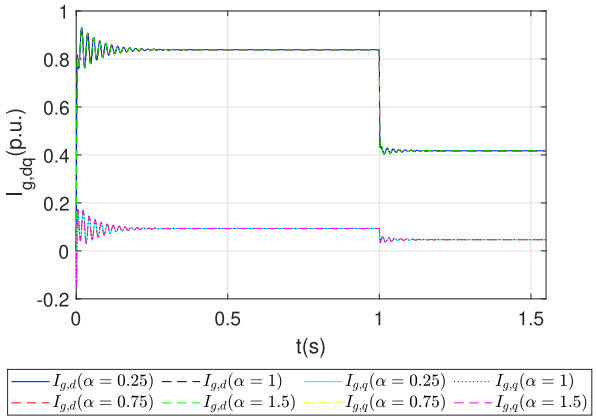

FIGURE 24. Simulation of FPRX2 in transient regime for $0 < \alpha < 2$.

the value of the feedback inductance, L_b, is modified in the next subsection.

6) FPRX2-CONTROLLED VSC CONNECTED TO A WEAK AC GRID

If a complementary feedback branch, $j\omega L_b$, is added to the FPRXC-controlled system, the grid current controller is transformed into FPRX2. When FPRX2-controlled system is implemented in a weak AC grid connection, being $L_b = 0.4$ mH, the $I_{g,d}$ and $I_{g,q}$ responses are stable for the entire range of α belonging to $0 < \alpha < 2$, as seen in Fig. 24.

However, the assigned value of L_b is not sufficient to improve the tracking capabilities of the FPRX2 controller, and $I_{g,d}$ and $I_{g,q}$ signals present tracking errors with respect to $I_{g,d,ref}$ and $I_{g,q,ref}$ setpoints. Nevertheless, the FPRX2 controller, unlike FPRX2, has an extra degree of freedom introduced by the $j\omega L_b$ branch. By modifying the value of L_b, the tracking of $I_{g,d,ref}$ and $I_{g,q,ref}$ setpoints can be improved, as presented in Fig.25.

In Fig.25, the effect of increasing the inductance of the complementary feedback branch from 0.4 to 1mH, is showed. The adequate tracked response of $I_{g,d}$ and $I_{g,q}$ to converge to $I_{g,d,ref}$ and $I_{g,q,ref}$ is obtained with $L_b = 0.8$ mH.

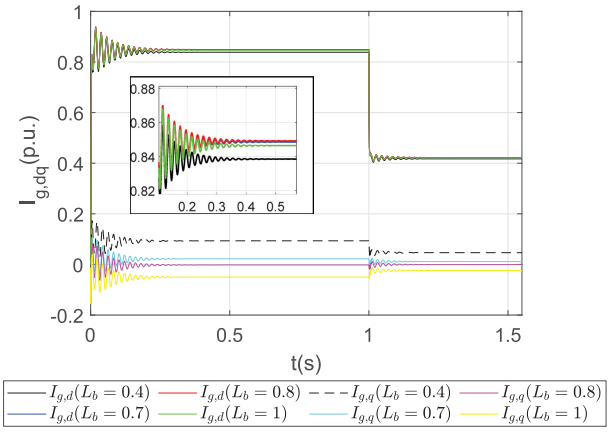

FIGURE 25. Simulation of FPRX2 in transient regime from $L_b = 0.4$mH to $L_b = 1$mH.

C. SENSITIVITY OF DYNAMIC RESPONSE ACCORDING TO A DIFFERENT SIZE OF THE AC FILTER INDUCTANCE

In this subsection, the transient dynamic response of the previous FPR-controlled MMC connected to a weak AC grid is analysed for a different size of the AC filter inductance, L_f. The impact of varying α and L_f is studied for the different FPR-controlled systems. Besides, the maximum L_f changes for each type of system is extracted in order not to compromise stability.

1) FIPR-CONTROLLED VSC CONNECTED TO A WEAK AC GRID

In the FIPR-controlled system, a $3L_f$ size for AC filter inductance is considered. For this new value, the transient behaviour of $I_{g,d}$ and $I_{g,q}$ signals is presented in Fig. 26 for a range of α values belonging to to $1 \leq \alpha \leq 1.15$.

As pinpointed in Fig. 26, the increase of α from 1 to 1.15 reduces the time response of $I_{g,d}$ and $I_{g,q}$ signals, for an AC filter inductance of $3L_f$.

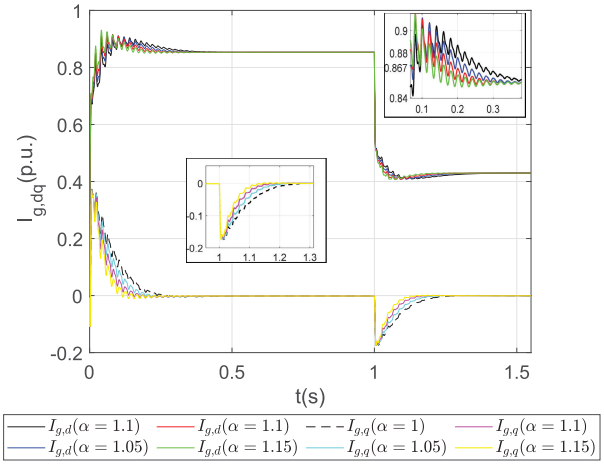

FIGURE 26. Simulation of FIPR for $3L_f$ for different α values.

2) FNIPR-CONTROLLED VSC CONNECTED TO A WEAK AC GRID

In the FNIPR-controlled system, a $3L_f$ size is also considered. For this new value, the transient behaviour of $I_{g,d}$ and $I_{g,q}$ signals is presented in Fig. 27, for α belonging to $1 \leq \alpha \leq 1.15$.

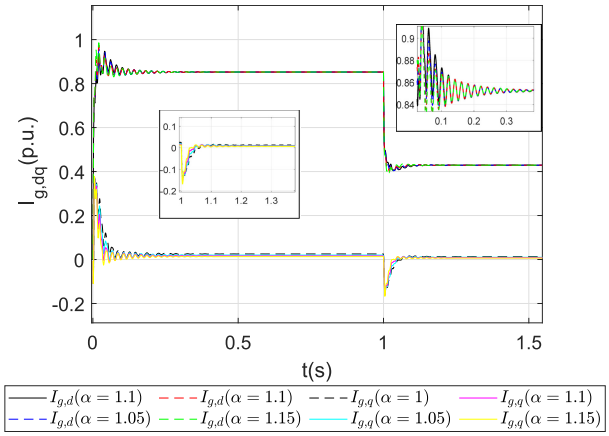

FIGURE 27. Simulation of FNIPR for $3L_f$ for different α values.

The increase of α from 1 to 1.15 does not alter the settling time of the $I_{g,d}$ and $I_{g,q}$ signals of the FNIPR-controlled system as much as those of the FIPR- controlled system, but slight dynamic improvements in the transient regime are observed.

3) FCVPR-CONTROLLED VSC CONNECTED TO A WEAK AC GRID

For the case of FCVPR-controlled system, the new L_f size has to be lower than with the FIPR and FNIPR-controlled systems, in order not to compromise stability. In Fig. 28, the $I_{g,d}$ and $I_{g,q}$ responses for $1.5L_f$ are showed when α belongs to $0.65 \leq \alpha \leq 0.75$ range.

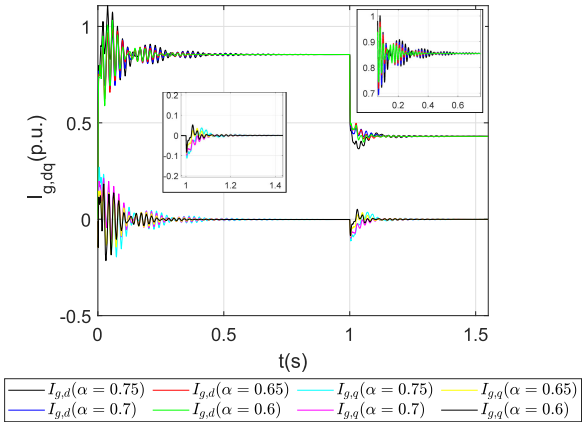

FIGURE 28. Simulation of FCVPR for $1.5L_f$ for different α values.

It can be seen in Fig. 28 that as far as α is decreased from 0.75 to 0.65, the transient response is slightly improved, as lower oscillation amplitude is observed in general.

It must be noted that $\alpha = 0.75$ is the closest value to the borders of stability, as greater values with the new L_f size, produce instability.

4) FPRXF-CONTROLLED VSC CONNECTED TO A WEAK AC GRID

In Fig. 29, the transient responses of $I_{g,d}$ and $I_{g,q}$ for a new size of $3L_f$ are presented for $1 \leq \alpha \leq 1.15$.

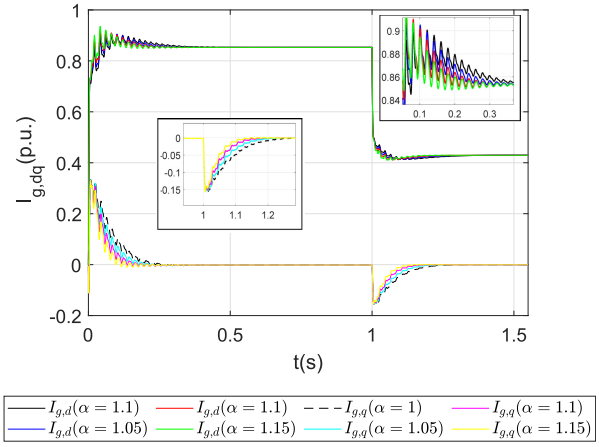

FIGURE 29. Simulation of FPRXF for $3L_f$ for different α values.

As with FIPR-controlled system, the increase of α from 1 to 1.15, reduces the settling time of the responses, at the cost of increasing the peak value. Nevertheless, intermediate values such as $\alpha = 1.1$, reduce the settling time and do not increase significanlty the oscillation amplitude.

5) FPRXC- AND FPRX2-CONTROLLED VSC CONNECTED TO A WEAK AC GRID

The extended form of FPRXC with the complementary feedback branch, i.e. FPRX2, has been chosen over FPRXC, as PRX2 allows for an extra degree of freedom introduced by the $j\omega L_b$ feedback branch.

As discussed before, by tuning $L_b = 0.8$ mH instead of 0.4 mH, the tracking errors in $I_{g,d}$ and $I_{g,q}$ are removed, whereas FPRXC does not track correctly. For this reason, $L_b = 0.8$ mH is initially chosen in order to study the transient response of $I_{g,d}$ and $I_{g,q}$ when a new size of $3L_f$ is set.

In Fig. 30, the $I_{g,d}$ and $I_{g,q}$ responses are showed for $\alpha = 1$ and $L_b = 0.8$ mH and tracking errors appear again. Then, a second case of $\alpha = 1$ with an increased L_b to 2.65 mH is showed, and it turns out that the tracking errors are removed.

The rest of $I_{g,d}$ and $I_{g,q}$ responses in Fig. 30 are provided with $L_b = 2.65$ mH, and α is varied from 0.5 to 1.75. In these cases, the variation of α does not have any significant effect on the improvement of the transient dynamic response.

D. COMBINED TUNING OF FRACTIONAL EXPONENT VALUES WITH OTHER CONTROL PARAMETERS

Along this Section different time-domain simulations of the grid currents at the PCC of each FPR-controlled MMC

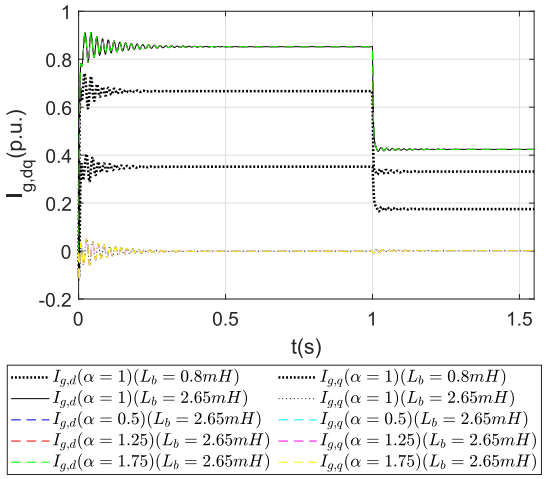

FIGURE 30. Simulation of FPRX2 for $3L_f$ for different α and L_b values.

have been obtained in order to compare their transient and steady-state behaviour.

As a result, the previous fractional exponent values of each FPR controller obtained by eigenvalue analysis have been verified by time domain simulations in a specific application, where the FPR-controlled MMC is connected to a weak AC grid. Several new tuning criteria have been detected while obtaining the simulations, given a set of fixed proportional and integral parameters.

For the FIPR and FPRXF controlled system, α values lower than 1 drive the system to instability as deduced from eigenvalue analysis and time-domain simulations, since the $I_{g,dq}$ currents diverged from their set-points. Nevertheless, whenever a first order damping term, $2\omega_c$s, was added in the denominator of the open-loop FIPR function, the eigenvalue trajectories remained in the left half-plane and the $I_{g,dq}$ currents were stable. In this sense, the transformation into FNIPR controller stabilised the eigenvalues of the FIPR controller and this was also shown in the time-domain transient simulations. However, the tracking capabilities of the FNIPR-controlled system with $\alpha < 1$ were poor, as the $I_{g,dq}$ currents did not match their setpoints $I_{g,dq,ref}$.

However, for $\alpha \geq 1$, FIPR-, FNIPR- and FPRXF-controlled systems the $I_{g,dq}$ currents were both stable and convergent to their respective setpoints, $I_{g,dq,ref}$. Besides, the increase of fractional exponent α between 1 and 2 improved the dynamic transient response in terms of oscillatory peak and amplitude reduction with respect to the controller tuned with $\alpha = 1$.

With regard to the FCVPR-controlled system, the eigenvalue analysis determined that for $\alpha \leq 1$, the system was stable and however, for $1 < \alpha < 1.25$ the system turned to be unstable. For greater values, i.e. $1.25 \leq \alpha < 2$, the system recovered the stability, but it was without considering the effects of a weak AC grid. In the time-domain simulations of a FCVPR-controlled system with $\alpha \leq 1$, the $I_{g,dq}$ currents were stable and convergent to their setpoints, $I_{g,dq,ref}$. In such case, the transient behaviour was improved as long as α was decreased from 1 to 0.25, in terms of oscillatory peak and amplitude reduction. For $\alpha > 1$, the $I_{g,dq}$ currents of the FCVPR-controlled system lost the stability and oscillated significantly. The effect of including a weak AC grid connection makes the system unstable also for $\alpha \geq 1.25$.

The FPRXC and FPRX2 controllers were reported to be stable for the entire range of α belonging to $0 < \alpha < 2$, according to the eigenvalue trajectory analysis. The time-domain simulations of the FPRXC and FPRX2-controlled systems also verified this and the effect of varying α did not change the transient behaviour significantly. However, the $I_{g,dq}$ currents did not match the setpoints, $I_{g,dq,ref}$. By tuning the L_b value of the feedback branch of PRX2 controller from 0.4 to 0.8 mH, the PRX2 controller managed to drive the $I_{g,dq}$ currents to match their setpoints again.

When a different L_f size is considered, the tuning of the fractional exponent has been reconsidered for each FPR-controlled system.

For FIPR-, FNIPR- and FPRXF-controlled systems, the new size of the AC filter inductance has been set to $3L_f$. With this new size, the increase of α from 1 to 1.15 changes the dynamic behaviour of the $I_{g,dq}$ signals. For FIPR- and FPRXF-controlled systems, $\alpha = 1$ and $\alpha = 1.15$, are the α values with greatest and lowest time response of $I_{g,dq}$ signals, respectively. However, $\alpha = 1.15$ is the case with greatest oscillation amplitude. Therefore, an intermediate value, $\alpha = 1.1$, presents a lower time response than with $\alpha = 1$ and lower oscillation amplitude than with $\alpha = 1.15$. In the case of FNIPR-controlled system, its performance is similar as with the FIPR or FPRXF controllers, but their effects while varying α are less noticeable.

In the case of FCVPR-controlled system, a new size of $1.5L_f$ has been set. With this new size, the decrease of α from 0.75 to 0.6 provides benefits in terms of stability, being the systems with $\alpha = 0.75$ and 0.6 those that present the greatest and lowest time response, respectively. However, since the oscillation amplitude is high at both extremes of the tested α interval, an intermediate $\alpha = 0.65$ is more convenient for the FCVPR-controlled system tuned with $1.5L_f$.

As for the FPRXC- and FPRX2- controlled systems, a new $1.5L_f$ size has been set. With this new size, the change in α does not have a significant effect on the dynamic transient response, and the $I_{g,dq,ref}$ references have been uncorrectly tracked again. In order to solve this issue, the L_b value of the complementary feedback branch has been increased from 0.8 mH to 2.65 mH and the final $I_{g,dq}$ currents match their references properly.

VII. CONCLUSION

A novel methodology for tuning diverse fractional order proportional resonant controllers in a weak AC grid environment has been proposed in this paper. In this methodology the role of fractional exponent, α, has been widely studied, as well as the combined tuning of α with other key control parameters, such as the damping frequency, ω_c,and the inductance

of complementary feedback branch, L_b. Appart from this, the influence of the AC filter size, L_f, on the dynamic transient response has been analysed.

By means of eigenvalue trajectory analysis, the impact of the fractional exponent, α, on the stability of each FPR control structure has been clarified. Besides, the range of α values reported by eigenvalue analysis have been verified via time-domain simulations in an application, where each FPR-controlled MMC is connected to a weak AC grid.

The time-domain simulations have shown the dynamic transient behaviour of different FPR control structures and has helped to build a tuning criteria to tune the fractional exponent, α, in combination with other control parameters ω_c or L_b to improve the transient responses of grid currents and the tracking capabilities of each FPR controller. Moreover, this analysis has been carried out with an increased L_f size, which pointed out minor resizings of the fractional exponent, α, and of the feedback branch inductance, L_b, to guarantee an adequate transient response.

APPENDIX A
PARAMETERS FOR EIGENVALUE ANALYSIS

A. GENERAL PARAMETERS COMMON TO EACH FPR CONTROLLER

$$R_f = 0.1\Omega$$
$$L_f = 18 \text{ mH}$$
$$\omega = 314.159 \text{ rad/s}$$

B. FIPR

$$k_p = 1.5$$
$$k_i = 50$$

C. FNIPR

$$k_p = 1.5$$
$$k_i = 50$$
$$\omega_c = 5 \text{ rad/s}$$

D. FCVPR

$$k_p = 1.5$$
$$k_i = 5000$$

E. FPRXF

$$k_p = 1.5$$
$$k_i = 50$$
$$L_b = 0.4 \text{ mH}$$

F. FPRXC

$$k_p = 11$$
$$k_i = 628$$

G. FPRX2

$$k_p = 11$$
$$k_i = 628$$
$$L_b = 0.4 \text{ mH}$$

APPENDIX B
AC GRID PARAMETERS

SCR_{PCC}	S_{PCC} (MVA)	$S_{AC,grid}$ (MVA)	R_{AC} (Ω)	L_{AC} (H)
2.34	1311	1300	5.7	0.182
1.47	825	800	9.3	0.292

APPENDIX C
CIRCULATING GRID CONTROL PARAMETERS

A. PROPORTIONAL INTEGRAL CONTROLLERS: PI_1 AND PI_2

Proportional gain $k_p = 10$
Integral gain $k_i = 100$

REFERENCES

[1] A. I. Elsanabary, G. Konstantinou, S. Mekhilef, C. D. Townsend, M. Seyedmahmoudian, and A. Stojcevski, "Medium voltage large-scale grid-connected photovoltaic systems using cascaded H-Bridge and modular multilevel converters: A review," *IEEE Access*, vol. 8, pp. 223686–223699, 2020, doi: 10.1109/ACCESS.2020.3044882.

[2] G. Liu, K. Anaya, and M. Pollitt, "Digitalisation and new business models in energy sector," Cambridge Judge Bus. School, Energy Policy Res. Group, Univ. Cambrigde, EPRG Working Paper 1920, 2019.

[3] M. Haro-Larrode, M. Santos-Mugica, P. Eguia, R. Rodriguez-Sanchez, and A. Gil-de-Muro, "Impact of proportional resonant controller parameters of VSC connected to AC grids with variable X/R characteristic on the small signal stability," *Int. J. Electr. Power Energy Syst.*, vol. 118, Jun. 2020, Art. no. 105746, doi: 10.1016/j.ijepes.2019.105746.

[4] F. Wilches-Bernal, J. Wold, and W. H. Balliet, "A method for correcting frequency estimates for synthetic inertia control," *IEEE Access*, vol. 8, pp. 229141–229151, 2020, doi: 10.1109/ACCESS.2020.3044583.

[5] G. Bergna-Diaz, S. Sanchez, and E. Tedeschi, "Port-Hamiltonian modelling of modular multilevel converters with fixed equilibrium point," in *Proc. 12th Int. Conf. Ecol. Vehicles Renew. Energ. (EVER)*, Monte Carlo, Monaco, Apr. 2017, pp. 1–12, doi: 10.1109/EVER.2017.7935911.

[6] J. A. Rohten, J. J. Silva, J. A. Munoz, F. A. Villarroel, D. N. Dewar, M. E. Rivera, and J. R. Espinoza, "A simple self-tuning resonant control approach for power converters connected to micro-grids with distorted voltage conditions," *IEEE Access*, vol. 8, pp. 216018–216028, 2020, doi: 10.1109/ACCESS.2020.3041528.

[7] R. N. Damas, Y. Son, M. Yoon, S.-Y. Kim, and S. Choi, "Subsynchronous oscillation and advanced analysis: A review," *IEEE Access*, vol. 8, pp. 224020–224032, 2020, doi: 10.1109/ACCESS.2020.3044634.

[8] D. Jovcic, L. Lamont, and K. Abbott, "Control system design for VSC transmission," *Electr. Power Syst. Res.*, vol. 77, no. 7, pp. 721–729, May 2007, doi: 10.1016/j.epsr.2006.06.011.

[9] S. Sanchez, G. Bergna, and E. Tedeschi, "Tuning of control loops for grid-connected modular multilevel converters under a simplified port representation for large system studies," in *Proc. 12th Int. Conf. Ecol. Vehicles Renew. Energ. (EVER)*, Monte-Carlo, Monaco, Apr. 2017, pp. 1–8.

[10] Y. Li, S. Yang, K. Wang, and D. Zeng, "Research on PI controller tuning for VSC-HVDC system," in *Proc. Int. Conf. Adv. Power Syst. Autom. Protection*, Beijing, China, Oct. 2011, pp. 261–264.

[11] A. Lesnicar and R. Marquardt, "An innovative modular multilevel converter topology suitable for a wide power range," in *Proc. IEEE Bologna Power Tech Conf. Process.*, Jun. 2003, p. 6.

[12] S. Rohner, S. Bernet, M. Hiller, and R. Sommer, "Modulation,losses, and semiconductor requirements of modular multilevel converters," *IEEE Trans. Ind. Electron.*, vol. 57, no. 8, pp. 2633–2642, Aug. 2010.

[13] G. Bergna-Diaz, D. Zonetti, S. Sanchez, R. Ortega, and E. Tedeschi, "PI passivity-based control and performance analysis of MMC multi-terminal HVDC systems," *IEEE J. Emerg. Sel. Topics Power Electron.*, vol. 7, no. 4, pp. 2453–2466, Dec. 2019, doi: 10.1109/JESTPE.2018.2889152.

[14] P. W. Lehn and S. Podrucky, "Small-signal modeling of power electronic converters with resonant controllers," in *Proc. Int. Conf. power Syst. Transients*, Kyoto, Japan, vol. 3, Jun. 2003, p. 6.

[15] R. Teodorescu, F. Blaabjerg, M. Liserre, and P. C. Loh, "Proportional-resonant controllers and filters for grid-connected voltage-source converters," *IEE Proc.-Electr. Power Appl.*, vol. 153, no. 5, p. 750, 2006, doi: 10.1049/ip-epa:20060008.

[16] N. Zhang, H. Tang, C. Yao, R. Ortega, and E. Tedeschi, "A systematic method for designing a PR controller and active damping of the LCL filter for single-phase grid-connected PV inverters," *Energies*, vol. 7, no. 6, pp. 3934–3954, Jun. 2014, doi: 10.3390/en7063934.

[17] L. Yang, X. He, P. Zhang, and S. Liu, "Control scheme and performance analysis of dual-frequency single-phase grid-connected inverter interfaced with weak and distorted grids," *IEEE Access*, vol. 8, pp. 178639–178650, 2020, doi: 10.1109/ACCESS.2020.3022106.

[18] F. de Bosio, M. Pastorelli, L. A. D. S. Ribeiro, M. S. Lima, F. Freijedo, and J. M. Guerrero, "Current control loop design and analysis based on resonant regulators for microgrid applications," in *Proc. 41st Annu. Conf. IEEE Ind. Electron. Soc.*, Nov. 2015, pp. 5322–5327, doi: 10.1109/IECON.2015.7392938.

[19] J. G. Hwang, P. W. Lehn, and M. Winkelnkemper, "A Generalized class of stationary frame current controllers for grid-connected AC–DC converters," *IEEE Trans. Power Del.*, vol. 25, p. 2742–2751, 2010, doi: 10.1109/TPWRD.2010.2045136.

[20] T. Ngo and S. Santoso, "Improving proportional-resonant controller for unbalanced voltage and frequency variation grid," in *Proc. IEEE/PES Transmiss. Distrib. Conf. Expo. (T&D)*, May 2016, pp. 1–5, doi: 10.1109/TDC.2016.7520071.

[21] B. Vinagre, I. Podlubny, A. Hernãindez, and V. Feliu, "Some approximations of fractional order operators used in control theory and applications," *Fractional Calculus Appl. Anal.*, vol. 3, pp. 231–248, Dec. 2010, doi: 10.1109/TPWRD.2010.2045136.

[22] A. Yáce, F. N. Deniz, and N. Tan, "A new integer order approximation table for fractional order derivative operators," *IFAC-PapersOnLine*, vol. 50, no. 1, pp. 9736–9741, Jul. 2017, doi: 10.1016/j.ifacol.2017.08.2177.

[23] H. Malek, S. Dadras, C. Yin, and Y. Chen, "Fractional order proportional-resonant controller," in *Proc. Annu. Amer. Control Conf. (ACC)*, Milwaukee, WI, USA, Jun. 2018, pp. 3086–3091, doi: 10.23919/ACC.2018.8431202.

[24] D. Heredero-Peris, C. Chillón-Antón, E. Sãinchez-Sãinchez, and D. Montesinos-Miracle, "Fractional proportional-resonant current controllers for voltage source converters," *Electr. Power Syst. Res.*, vol. 168, pp. 20–45, doi: 2019,10.1016/j.epsr.2018.09.014.

[25] D. Heredero-Peris, E. Sanchez-Sanchez, C. Chillon-Anton, D. Montesinos-Miraclesss, and S. Galceran-Arellano, "A novel fractional proportional-resonant current controller for voltage source converters," in *Proc. 18th Eur. Conf. Power Electron. Appl.*, Karlsruhe, Germany, Sep. 2016, pp. 1–10, doi: 10.1109/EPE.2016.7695305.

[26] E. A. Mohamed, E. M. Ahmed, A. Elmelegi, M. Aly, O. Elbaksawi, and A.-A.-A. Mohamed, "An optimized hybrid fractional order controller for frequency regulation in multi-area power systems," *IEEE Access*, vol. 8, pp. 213899–213915, 2020, doi: 10.1109/ACCESS.2020.3040620.

[27] V. Mihaly and E. Dulf, "Novel fractional order controller design for first order systems with time delay," in *Proc. IEEE Int. Conf. Autom., Qual. Test., Robot. (AQTR)*, Cluj-Napoca, Romania, May 2020, pp. 1–4, doi: 10.1109/AQTR49680.2020.9129995.

[28] T. Yuan, M. Zheng, K. Zhang, and T. Huang, "Fractional-order PID controllers for stabilization of fractional-order time delay systems based on region stability," in *Proc. Chin. Control Decis. Conf. (CCDC)*, Shenyang, China, Jun. 2018, pp. 6633–6638, doi: 10.1109/CCDC.2018.8408298.

[29] I. Birs, C. Muresan, D. Copot, I. Nascu, and C. Ionescu, "Design and practical implementation of a fractional order proportional integral controller (FOPI) for a poorly damped fractional order process with time delay," in *Proc. 7th Int. Conf. Control, Mechatronics Autom. (ICCMA)*, Delft, The Netherlands, Nov. 2019, pp. 56–61, doi: 10.1109/ICCMA46720.2019.8988655.

[30] D. S. Acharya, B. Sarkar, and D. Bharti, "A fractional order particle swarm optimization for tuning fractional order PID controller for magnetic levitation plant," in *Proc. 1st IEEE Int. Conf. Meas., Instrum., Control Autom. (ICMICA)*, Kurukshetra, India, Jun. 2020, pp. 1–6, doi: 10.1109/ICMICA48462.2020.9242792.

[31] B. Chipipop and D. Puangdownreong, "Designing of fractional order PID controller for stable fractional order system," in *Proc. Joint Int. Conf. Digit. Arts, Media Technol.*, Nan, Thailand, Jan. 2019, pp. 77–80, doi: 10.1109/ECTI-NCON.2019.8692234.

[32] B. Chipipop and D. Puangdownreong, "Designing of fractional order PID controller for unstable fractional order system," in *Proc. Joint Int. Conf. Digit. Arts, Media Technol.*, Nan, Thailand, Jan. 2019, pp. 81–84, doi: 10.1109/ECTI-NCON.2019.8692259.

[33] S. Pashaei and F. Hashemzadeh, "A new fractional-order control method for robust synchronization between fractional-order uncertain permanent magnet synchronous motors," in *Proc. 27th Iranian Conf. Electr. Eng. (ICEE)*, Yazd, Iran, Apr. 2019, pp. 904–908, doi: 10.1109/IranianCEE.2019.8786465.

[34] M. Allagui, N. Yousfi, N. Derbel, and P. Melchior, "Robust fractional order controller and prefilter tuning in MIMO motion control," in *Proc. 15th Int. Multi-Conference Syst., Signals Devices (SSD)*, Yasmine Hammamet, Tunisia, Mar. 2018, pp. 122–126, doi: 10.1109/SSD.2018.8570604.

[35] G. Maione, "Continued fractions approximation of the impulse response of fractional-order dynamic systems," *IET Control Theory Appl.*, vol. 2, no. 7, pp. 564–572, Jul. 2008, doi: 10.1049/iet-cta:20070205.

[36] A. X. R. Irudayaraj, N. I. A. Wahab, M. G. Umamaheswari, M. A. M. Radzi, N. B. Sulaiman, V. Veerasamy, S. C. Prasanna, and R. Ramachandran, "A Matignon's theorem based stability analysis of hybrid power system for automatic load frequency control using atom search optimized FOPID controller," *IEEE Access*, vol. 8, pp. 168751–168772, 2020, doi: 10.1109/ACCESS.2020.3021212.

[37] S. K. Choudhary, "Stability and performance analysis of fractional order control systems," *WSEAS Trans. Syst. Control*, vol. 9, pp. 438–444, Dec. 2014, doi: 10.5281/zenodo.2590916.

MARTA HARO-LARRODE received the M.Sc. degree in industrial engineering with specialization in electric power systems from the University of Zaragoza, Spain, in 2012, the master's degree in renewable energy from the CIRCE Institute, Zaragoza, Spain, in 2013, and the Ph.D. degree in electric power engineering from the University of the Basque Country (UPV/EHU), Bilbao, Spain, in 2020, which was financed by the Tecnalia Research and Innovation.

She is currently an Assistant Professor with the University of Zaragoza. Her research interests include the modeling, control, and stability analysis of electric power systems with high content of renewable energy.

GILBERT BERGNA-DIAZ (Member, IEEE) received the electrical power engineering degree from the Universidad Simón Bolívar, Caracas, Venezuela, in 2008, the master's degree (research) in electrical energy from the École Supérieure d Électricité (Supélec), Paris, France, in 2010, and the joint Ph.D. degree in electric power engineering from École Centrale Supélec and the Norwegian University of Science and Technology (NTNU), Trondheim, Norway, in 2015. In 2014, he joined SINTEF Energy Research as the Research Scientist, where he was involved in modeling, analysis, and control of HVdc transmission systems. In 2016, he joined the Department of Electric Power Engineering, NTNU, as a Postdoctoral Research Fellow, where he was involved in energy-based modeling and nonlinear control of multiterminal HVdc grids. Since 2019, he has been serving as an Associate Professor with the Department of Electric Power Engineering, NTNU.

PABLO EGUIA (Member, IEEE) was born in Bilbao, Spain, in 1973. He received the Ph.D. degree in electrical engineering from the University of the Basque Country, Bilbao, Spain, in 2007. He is currently an Assistant Professor with the Department of Electrical Engineering, University of the Basque Country UPV/EHU. He is also the Leader of the GISEL Research Group. His research interests include power systems analysis and simulation, integration of renewable generation, and power system control and protection.

MAIDER SANTOS-MUGICA received the M.S. and Ph.D. degrees in electronic and automatic engineering from the University of Mondragon Unibertsitatea, Spain, in 2003 and 2007, respectively. Since 2007, she has been with Tecnalia, Spain, where she is currently a Research Engineer with the Energy Unit. She worked in many projects related to power control systems for wind and wave power grid integration. She participated in about ten research projects supported by public institutions and private companies. Nowadays, she works in several projects related to ocean energy and offshore wind grid integration.